Neuroinform (2010) 8:83–100
DOI 10.1007/s12021-010-9067-9

Automatic Robust Neurite Detection and Morphological Analysis of Neuronal Cell Cultures in High-content Screening

Chaohong Wu · Joost Schulte · Katharine J. Sepp · J. Troy Littleton · Pengyu Hong

Abstract Cell-based high content screening (HCS) is becoming an important and increasingly favored approach in therapeutic drug discovery and functional genomics. In HCS, changes in cellular morphology and biomarker distributions provide an information-rich profile of cellular responses to experimental treatments such as small molecules or gene knockdown probes. One obstacle that currently exists with such cell-based assays is the availability of image processing algorithms that are capable of reliably and automatically analyzing large HCS image sets. HCS images of primary neuronal cell cultures are particularly challenging to analyze due to complex cellular morphology. Here we present a robust method for quantifying and statistically analyzing the morphology of neuronal cells in HCS images. The major advantages of our method over existing software lie in its capability to correct non-uniform illumination using the contrast-limited adaptive histogram equalization method; segment neuromeres using Gabor-wavelet texture analysis; and detect faint neurites by a novel phase-based neurite extraction algorithm that is invariant to changes in illumination and contrast and can accurately localize neurites. Our method was successfully applied to analyze a large HCS image set generated in a morphology screen for polyglutamine-mediated neuronal toxicity using primary neuronal cell cultures derived from embryos of a *Drosophila* Huntington's Disease (HD) model.

Keywords High content screening · Neurite detection · Neuromeres · Gabor filter · Phase symmetry · Huntington's Disease

High throughput automated fluorescent microscopy of cell culture preparations has opened new avenues for discovery in the fields of functional proteomics (Liebel et al. 2003; Eggert et al. 2004; Muller et al. 2005; Pelkmans et al. 2005; Sonnichsen et al. 2005; Wheeler et al. 2005; Neumann et al. 2006; Wollman and Stuurman 2007; Peng 2008), small-molecule screening (Eggert et al. 2004; Mitchison 2005; Eggert and Mitchison 2006; Carpenter 2007), and drug profiling (Perlman et al. 2004). In high-content screening (HCS), multiple images are collected per microplate well, often at one or more wavelengths (multiplexing), and processed by image analysis algorithms to extract specific cellular features from the complex cellular patterns. For example, when cells are appropriately labelled with vital dyes or fluorescent markers, algorithms can be developed to quantify cell size, cell number, the position of cellular organelles, or even the distributions of proteins at the subcellular level (Boland et al. 1998; Boland and Murphy 1999; Murphy et al. 2000; Boland and Murphy 2001; Chen and Murphy 2006). Automatic image analysis is of critical importance to HCS as it enables rapid quantification and statistical analysis of large HCS image sets, which is not feasible manually. Moreover, manual analysis is prone to investigator error and bias, which can be eliminated with automation (Wollman and Stuurman 2007). Recently, HCS

C. Wu · P. Hong (✉)
Department of Computer Science, Brandeis University,
Waltham, MA 02454, USA
e-mail: hongpeng@brandeis.edu

J. Schulte · K. J. Sepp · J. T. Littleton
The Picower Institute for Learning and Memory,
Departments of Biology and Brain and Cognitive Sciences,
Massachusetts Institute of Technology,
Cambridge, MA 02139, USA

K. J. Sepp
Department of Genetics, Harvard Medical School,
Boston, MA 02115, USA

has been adopted to conduct analysis of primary neurons which have highly complex cellular morphologies and branching patterns. This type of analysis has been a powerful methodology in RNA interference (RNAi) screening experiments to identify genes that are important for neuronal development, physiology and disease (Dragunow 2008; Sepp et al. 2008). Such studies are expected to be an increasingly utilized approach in drug discovery as neuronal morphology can be used as an assay for cell health.

Noise and complex signals make it challenging to quantify neurites and neuromeres, which are two essential morphological elements that relate to neuronal health status. For example, noise can arise from non-neuronal cells, cell debris, or limitations in the sensitivity of charge-coupled device (CCD) cameras that are commonly used to collect images. The signal levels of key neurites can be very weak because of various factors, including variations in the thickness of the neurites, sub-optimal focus plane established by automated microscopy, 3-dimensional nature of the cell cultures, and inadequate exposure time lengths. In general, microscope settings for a screen are established on the basis of what is optimal for an average well of a multiwell screening plate. However, cell profiles in some wells may be significantly different in marker intensities, which can lead to under- or over-exposure of collected images. Image analysis must take this variability into account to quantify and analyze all screening wells.

Several methods have recently been proposed for detecting neurites in microscopy images. Nevertheless, they have limited use for neuronal HCS assays for various reasons. Meijering et al. (2004) developed a semi-automatic searching-based algorithm for tracing neurites, which requires users to manually identify neurite start and end points. In this method, neurites are extracted by optimizing an energy function based on second-order directional derivatives. Although this method works well for noisy and discontinuous line structures, it has difficulty detecting neurites with low contrast. In addition, it requires nontrivial manual inputs from users, and is therefore not feasible for high-throughput HCS studies. Zhang et al. (2007) improved the algorithm of Meijering et al. (2004) by incorporating automatic neurite endpoint detection. Nevertheless, the accuracy of endpoint detection is limited in noisy images with non-uniform backgrounds. Al-Kofahi et al. (2002) proposed an efficient neurite tracing algorithm that first determines the seed points of neurites and then extends them into complete neurites by exploiting pixels near line structures. In this algorithm, candidate seed points are first produced by line searches over a coarse grid. Final seed-points are then obtained through elimination of unfit candidates. A median kernel template is used in the improved version of this algorithm to deal with broken/discontinuous segments, discontinuous boundaries, impulsive noise and curvature (Al-Kofahi et al. 2003). However, the method to estimate local directions is sensitive to noise, which may affect the results. Furthermore, it requires the intensity of a candidate point to be higher than a threshold defined as the summation of the median pixel intensity and the standard deviation around the median. As such, important seed-points for long faint neurites or neurites in non-uniform backgrounds may go undetected.

Some neurite extraction methods (Narro et al. 2007; Vallotton et al. 2007; Broser et al. 2008; Pool et al. 2008) first binarize images into foregrounds and backgrounds by using a threshold that is determined either automatically or manually. Simple morphological operations are then applied to remove speckles and artifacts in the foreground. Finally, neurites are obtained by skeletonising the foregrounds. In practice, choosing an appropriate global binarization threshold can be difficult, especially when many faint neurites exist. Hence, the above methods work well on assumed "clean" images (Pool et al. 2008) which do not include a significant number of faint neurites. In addition, the binarization step can break strong neurites if they contain faint segments. To correct this shortcoming, NeuronMetrics (Narro et al. 2007) offers a nice function that attempts to fill in gaps of skeletons. Nevertheless, NeuronMetrics requires manual neurite selection, noise elimination, and cell body demarcation (Narro et al. 2007), which is not practicable for high-throughput screening. Recently, Sun and Vallotton (2009) developed an automatic linear feature detection algorithm using multiple directional non-maximum suppression with symmetry checking, which can be applied to neurite detection. Their method detects neurite central points as the maximums in the local intensity profiles defined by a set of linear windows. This algorithm is very fast and has been implemented in HCA-Vision (http://www.hca-vision.com/). However, it can be very sensitive to noise, non-neuronal cells in mixed culture preparations, or cell debris.

We have developed an image processing pipeline that can efficiently extract and quantify neurites and other cellular morphology attributes relevant to the analysis of HCS images of neuronal cell cultures. The method responds well to the challenges (e.g., non-uniform image backgrounds, large variation in image intensities, and complex morphology of neuronal cell cultures) in analyzing noisy fluorescent microscopy images of typical HCS neuronal assays using small molecule libraries or gene knock-down probes. To overcome these challenges, the pipeline performs several key processing steps (Fig. 1), including background correction and contrast enhancement, neuromere segmentation, neurite seed line generation, and ultimately neurite tracing. We have compared our approach with two state-of-art software packages that have automatic neurite-tracing capacities, HCA-Vision and NeuriteIQ (http://www.cbi-tmhs.org/NeuriteIQ/index.htm), and found that our approach made fewer errors in

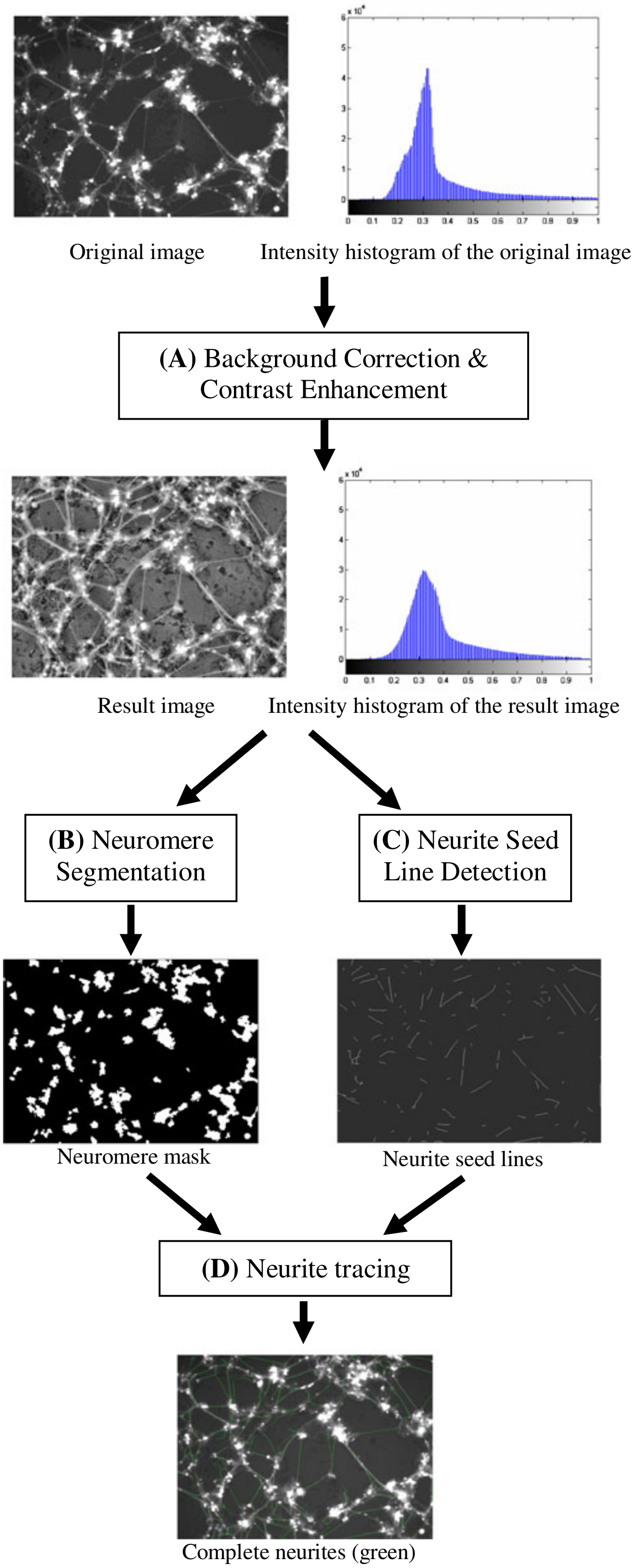

Fig. 1 Processing HCS images of neuronal cell cultures. **A** Background correction and contrast enhancement using the contrast-limited adaptive histogram equalization method. The processed image has a more uniform background distribution and better local contrast. **B** Neuromere segmentation. The white mask denotes neuromeres of the image. **C** Seed line generation. Seed lines corresponding to reliable neurite segments are extracted by analyzing the phase map. **D** Neurite tracing. Complete neurites (in green) are generated by extending seed lines

neurite extraction, and was better equipped to detect faint neurites, as well as neurites in noisy backgrounds containing cell debris. Our approach also provides a set of neuronal morphology metrics and a statistical analysis procedure that can be used to compare morphological profiles of different treatment conditions and thus identify hits. To test the robustness of our approach, we used our method to define morphological differences in primary neuronal cell cultures derived from a *Drosophila* Huntington's Disease (HD) model. HD is an autosomal dominant neurodegenerative disorder resulting from the expansion of a polyglutamine (polyQ) stretch in the coding region of the Huntington (Htt) protein. Expansion of the polyQ stretch beyond 35 glutamines results in aggregation of the mutant protein and neuronal degeneration, leading to motor dysfunction, dementia and ultimately death (Kimura et al. 2007). There are no known cures for HD, making it an important target for high-throughput screens to identify potential therapeutic agents that can suppress disease pathology. As a first step towards this goal, we have used our approach to define morphological differences between non-pathogenic (Htt-Q15) and pathogenic (Htt-Q138) versions of the protein expressed in *Drosophila* neuronal cultures. We examined the ability of our approach to identify Htt-Q138 protein aggregation, and its subsequent effects on neuronal morphology. These parameters can now be employed in high-content chemical-compound screening to identify drug-suppression of aggregation or morphological degeneration, allowing new possibilities for HCS in neuronal-based models.

Methods

Drosophila HD Data Set

Images used to develop and test our automatic neurite detection and morphological analysis methodology were obtained from a partial HCS image set of primary neuronal cultures derived from a *Drosophila* HD model (unpublished data). In HD primary neuronal cultures expressing elav-GAL4, neuronal membranes were labelled with green fluorescent protein (UAS-CD8-GFP), and pathogenic (UAS-Q138-mRFP) or non-pathogenic (UAS-Q15-mRFP) human Huntingtin protein was labelled with monomeric red fluorescent protein (mRFP) using a chimeric Huntingtin-mRFP construct. The HD primary cultures were obtained from early stage embryo homogenates and contained multiple unlabelled cell types including muscles, glia, and

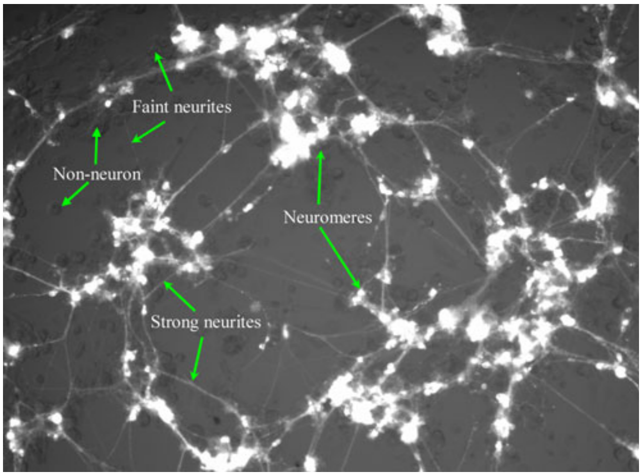

Fig. 2 A typical HCS image of neuronal cell cultures. Noise in the image can come from non-neuronal cells, cell debris, and illumination changes. Both the intensities and the widths of neurites vary greatly. Although some neurites appear to be faint due to imaging artefacts, they can be long and straight, and hence are important features indicating healthy connections between neuronal cells. The large variation in neurite width (range from 1 to 8 pixels) makes it very difficult to accurately localize them using traditional edge detectors. Neuromeres (cell colonies) consist of neuronal cell bodies and their surrounding ecology substances

hemocytes that contributed to image background. Cultures were plated on 384-well optical bottom plates (Costar cat. No. 3712) and treated with 100 nL of compound (~1 mM to ~15 mM stocks) in a 50 uL assay volume. Mature cultures were imaged with an ImageXpress$^{\mathrm{MICRO}}$ robotic microscope (Molecular Devices, Sunnyvale, CA) using a 10× objective, and FITC/Cy3 filter sets, a gain=2, and binning=1. Images are 1392×1040 pixels, or 897×670 micrometers, and have a resolution of 0.645 micrometers/pixel. Autofocusing was laser-based to locate the bottom of the multiwell plate, and then image-based over a 48 micrometer range to resolve fluorescently labelled neurons. The GFP and mRFP channels were imaged at the same focal plane, with exposure times of 850 and 400 ms respectively. Three sites were imaged per well for each treatment group, and the screen was done in duplicate. In total, ~11000 image pairs (GFP and mRFP) were collected under ~1800 treatment conditions, plus an additional 500 control image pairs. Eight images were randomly selected from the HD image set to tune the parameters of our method, which we report below.

Background Correction and Contrast Enhancement

The HD screen image set is diverse and images contain a variety of cellular structures, noise, and complex signals (Fig. 2). There exists a significant variance in the background of the HCS neuronal cell culture images (Fig. 3a). The intensity levels of the background in the centre of an image can be comparable to those of neurites close to the image boundaries. Hence it is necessary to perform background correction. The background correction method must also avoid over-enhancement of noise, over-saturation, and the elimination of neurites in nearly homogeneous regions. We chose the contrast-limited adaptive histogram equalization (CLAHE) method (Zuiderveld 1994) for background correction and to improve local contrast (Figs. 1a, 3, and 4).

CLAHE divides each image into small tiles (16×16 pixels in this study). Histogram equalization is performed within each tile. Neighbouring tiles are refined using bilinear interpolation to eliminate artificially induced boundaries. CLAHE restricts the slope of the intensity mapping function by clipping the height of the histogram. A higher “clip level” value will result in more significant contrast enhancement. However, the noise level increases concomitantly. Mathematically, CLAHE finds a monotonic gray-level intensity transformation such that the cumulative output density must equal the cumulative probability

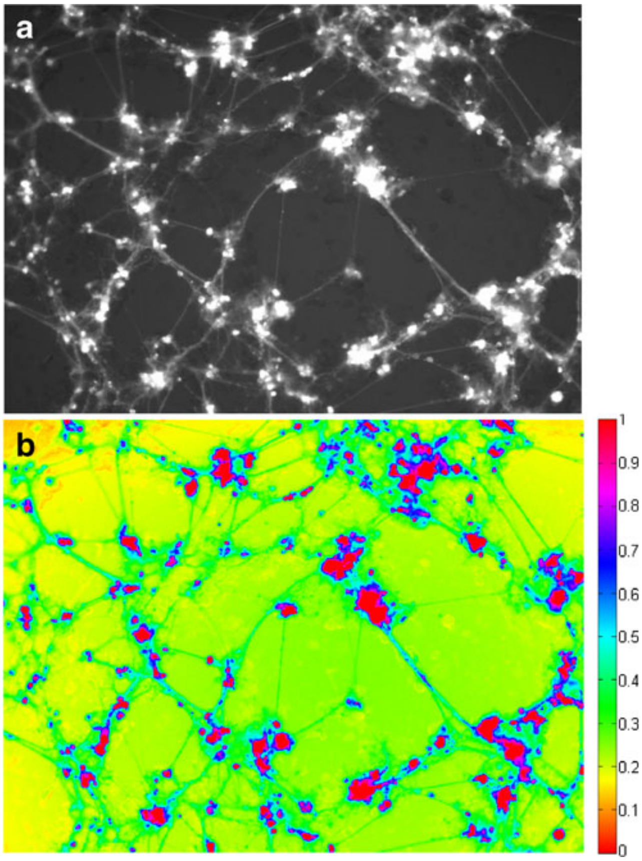

Fig. 3 Background variance of HCS neuronal cell culture images. **a** A typical gray-level HCS neuron cell culture image. **b** The pseudo-colour image of (**a**), where intensity values are indexed to the values of the hue component of the hue-saturation-value (HSV) colour model. The intensity values of neurites near the image boundaries are comparable to those of the background in the centre of the same image

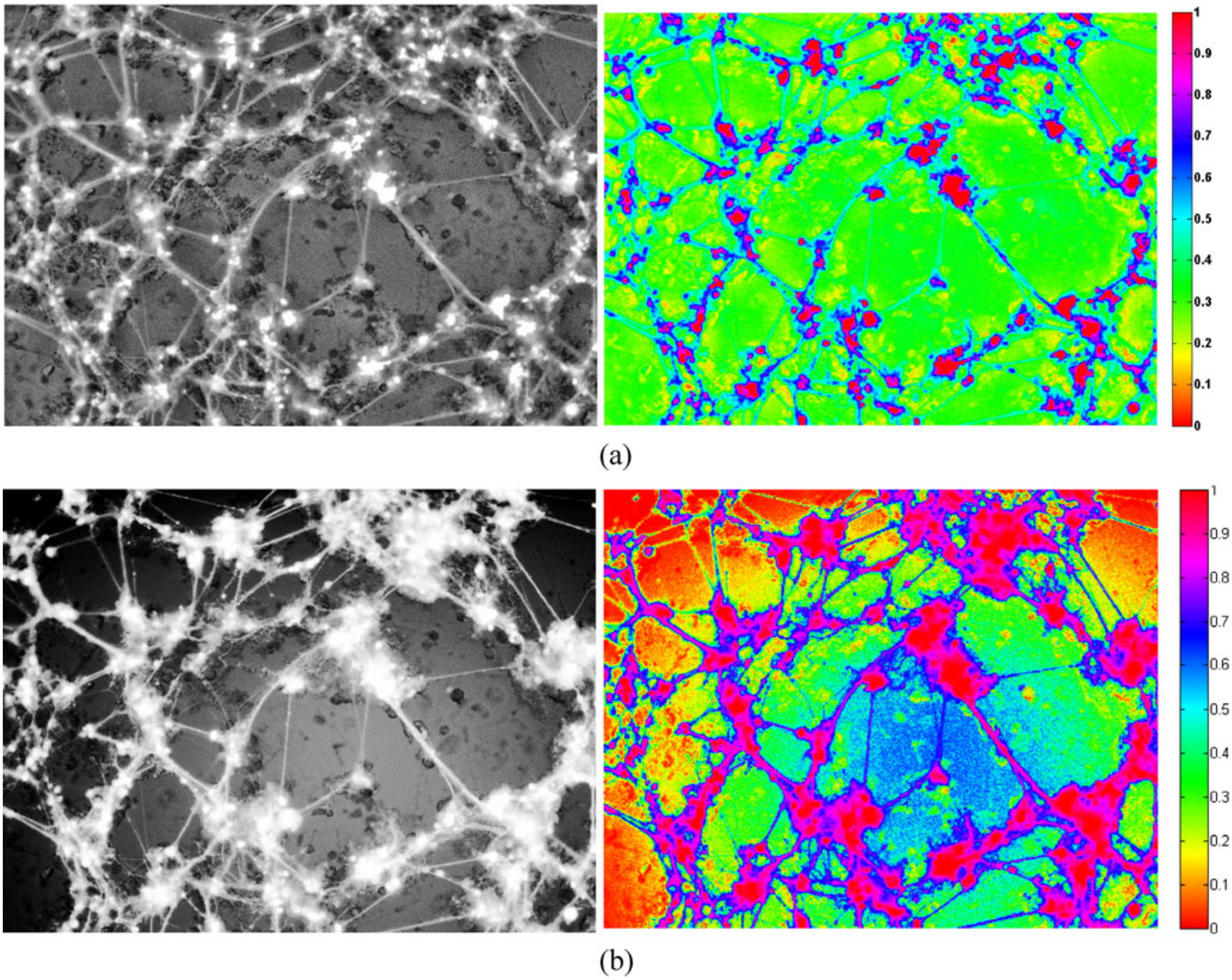

Fig. 4 Background correction and contrast enhancement. **a** The resulting image of Fig. 3a after background correction and contrast enhancement using the contrast-limited adaptive histogram equalization method (CLAHE). The left is the gray level image. The right is the pseudo-colour image, where intensity values are indexed to the values of the hue component of the hue-saturation-value (HSV) colour model. After enhancement, the background is more uniform (compared to Fig. 3b). It is also visually easier to distinguish non-neuronal signals from neuronal signals. **b** The results (left–gray level, right–pseudo colour) of the global histogram equalization method

distribution of the input image. A *Rayleigh distribution* is used as the transformation function in CLAHE:

$$y = y_{\min} + \left[2\alpha^2 \ln\left\{\frac{1}{1 - P_{input}(x)}\right\}\right]^{1/2} \tag{1}$$

where y is the output intensity level, $y_{\min}$ is the low bound, α is a parameter and was set to 0.4 for the analysis, x is the input intensity level, and $P_{input}(x)$ is the cumulative probability of the input image. The output probability density can then be derived as:

$$p(y) = \frac{y - y_{\min}}{\alpha^2} \exp\left\{-\frac{(y - y_{\min})^2}{2\alpha^2}\right\} \text{ for } y \geq y_{\min} \tag{2}$$

CLAHE may generate artefacts especially in the regions of high gray-level intensity gradients, which can be eliminated by using a low-pass filter to exclude high frequency components in the background-corrected images. Figure 4 compares the result using CLAHE and that using a global histogram equalization function “histeq” in Matlab.

Neuromere Segmentation

Neuromeres (Seecof et al. 1973; Fredieu and Mahowald 1989) are clusters of 6–20 neural cell bodies associated with glial cells. It is essential to segment out neuromeres prior to neurite tracing because their complicated texture can compromise neurite extraction efforts and lead to false or erroneous detection of neurites. In addition, neuromeres must be segmented out without removing too many neurites radiating from their perimeters because these perimeter neurites are important components of morphological profiles. Neuromeres are visually complex in the HD primary neuronal cultures analyzed. In neuromeres, the neuronal cell bodies are GFP-positive, while their associated support cells are not labelled. Although neuronal cell bodies usually correspond to high intensity regions in the images, the closely associated support cells and the 3-D nature of the cell culture complicate the gray-scale profiles of neuromere distal regions. As a result, neuromere pixel intensities span a wide spectrum with the lower end being close to background and faint neurites. The neuromere perimeters are irregular, and are difficult to define quantitatively in a geometrical manner. The high intensity portions of neuromeres can be easily and reliably extracted by using the Otsu method (Otsu 1979), which calculates a threshold to separate the foreground from the background so that their intra-class variance is minimal. However, this pure Otsu method works poorly for segmenting complete neuromeres.

Our method segments neuromeres by analyzing local image texture information using a bank of Gabor filters (Daugman 1985; Grigorescu et al. 2002) (Figs. 1b and 5). Each Gabor filter captures the characteristics of local texture in a certain direction. If an image region contains neuromeres, the values of some Gabor features in that region will be larger than other Gabor feature values. All the Gabor feature values in a homogenous background block should be similar to each other. Therefore, the standard deviation of the Gabor feature values can be used to generate a neuromere mask for an image.

A Gabor filter is composed of a Gaussian envelope modulated with a sinusoid of the frequency f along the orientation θ_k. The value of θ_k is defined as $\pi(k-1)/orient$,

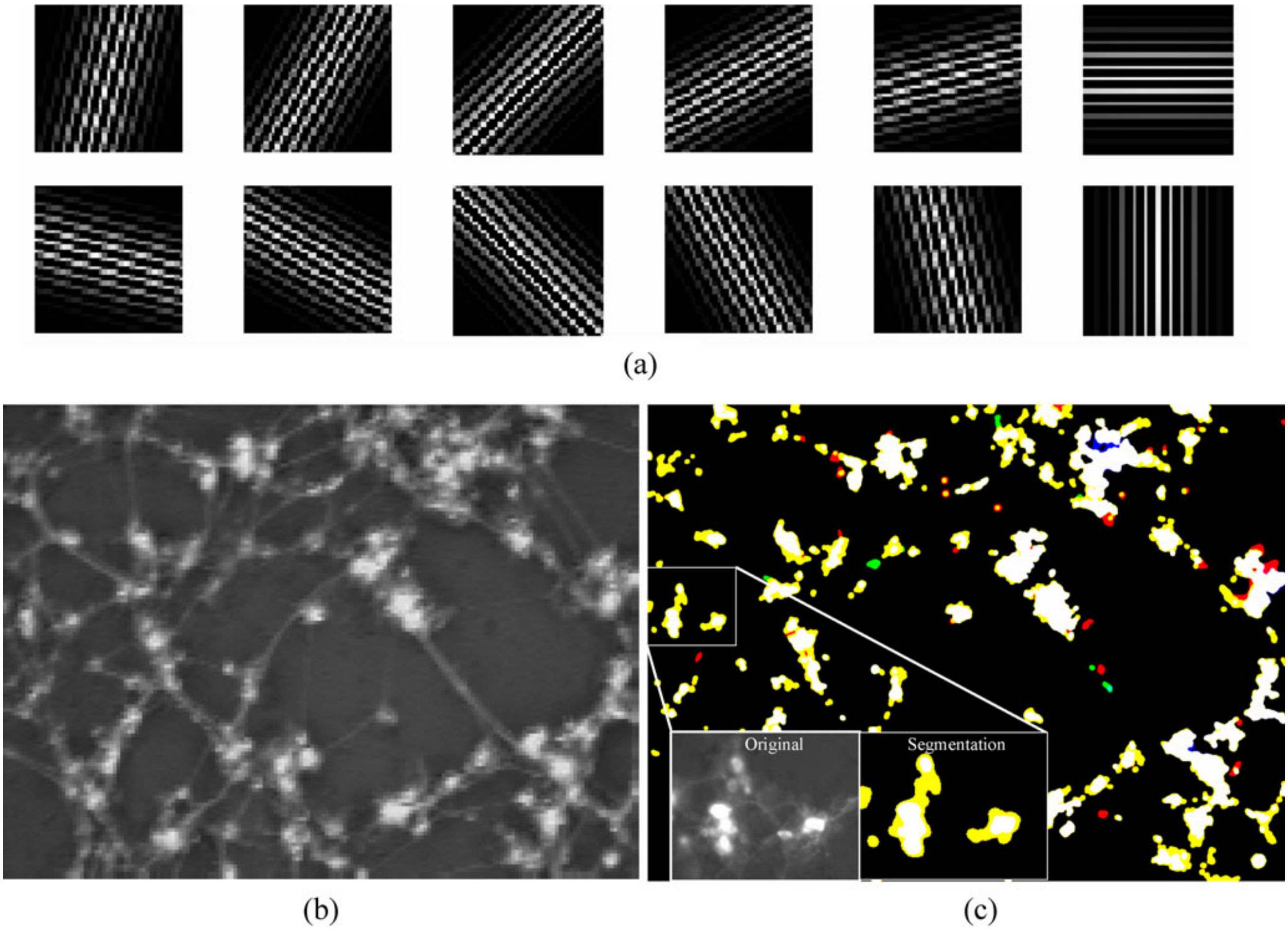

Fig. 5 Neuromere segmentation. **a** A bank of Gabor filters. Each image represents a Gabor filter in spatial domain. **b** The standard deviation of Gabor responses of Fig. 3a. **c** The neuromere segmentation results obtained from: manual segmentation (red), the proposed texture-based method (green), and the pure Otsu thresholding (blue). A region is in white if it was detected by all three methods. The bottom-right is a zoom-in of a region for clearer view

where *orient* represents the number of total orientations and $k=1, ..., orient$. The Gabor filter in the spatial domain is defined as:

$$g(x,y;f,\theta,\psi,\sigma_x,\sigma_y) = \frac{1}{2\pi\sigma_x\sigma_y} \times \exp\left(-\frac{1}{2}\left(\frac{x_r^2}{{\sigma_x}^2}+\frac{y_r^2}{\sigma_y^2}\right)\right) \times \exp(2\pi jfx_r+\psi) \tag{3}$$

where $x_r = x\cos\theta + y\sin\theta$, $y_r = -x\sin\theta + y\cos\theta$, f denotes the radial frequency of the Gabor function, the Gaussian envelope along the x and y axes is controlled by the space constants σ_x and σ_y. The ratio between σ_x and σ_y specifies the ellipticity of the support of the Gabor function, and the phase offset ψ denotes the symmetricality.

We used only the real components of the Gabor functions and set f, σ_x, σ_y, and ψ to 0.125, 6, 6, and $\pi/18$, respectively. The Gabor filter responses in the spatial domain and the spatial frequency domain are respectively given by:

$$R(x,y;f,\theta,\psi,\sigma_x,\sigma_y) = \frac{1}{2\pi\sigma_x\sigma_y} \times \exp\left(-\frac{1}{2}\left(\frac{x_r^2}{{\sigma_x}^2}+\frac{y_r^2}{\sigma_y^2}\right)\right) \times \cos(2\pi fx_r+\psi) \tag{4}$$

$$G(u,v) = \exp\left\{-\frac{1}{2}\left[\frac{(u-f)^2}{\sigma_u^2}+\frac{v^2}{\sigma_v^2}\right]\right\} + \exp\left\{-\frac{1}{2}\left[\frac{(u+f)^2}{\sigma_u^2}+\frac{v^2}{\sigma_v^2}\right]\right\} \tag{5}$$

Eighteen directions were used in analyzing our data set. Twelve of those are visualized in Fig. 5a. For each image block of size $W\times W$ centred at (x_0, y_0), the magnitude of a Gabor feature in direction k can be calculated by:

$$\Gamma_k(x,y;f,\theta,\psi,\sigma_x,\sigma_y) = \left|\sum_{x_0=-\frac{W}{2}}^{\frac{W}{2}-1}\sum_{y_0=-\frac{W}{2}}^{\frac{W}{2}-1} I(X+x_0,Y+y_0)R(x_0,y_0;f,\theta,\psi,\sigma_x,\sigma_y)\right| \tag{6}$$

We set the window size to 16×16 pixels in our experiment and used the standard deviation of the Gabor responses to characterize the complexity of local texture (an example is illustrated in Fig. 5b). An initial neuromere mask is first generated by applying the Otsu thresholding method (Otsu 1979) to the standard deviation map. The mask is refined by a morphological opening operation (González and Woods 2007) using a disk structuring element with radius 5 pixels to remove slim regions corresponding to noise and neurite segments. Using the neuromere mask labelled manually as the baseline, we compared the ability of our texture-based method to segment neuromeres with that of the pure Otsu thresholding method (Fig. 5c). The manual segmentation was carried out by two of the authors, who are experts in neuronal cell culture (J.S. and K.S.). The result of the pure Otsu thresholding method was refined to remove noise and slim regions using the same image opening operation used in our texture-based approach. From this analysis, we found that our texture-based method detected 96.5% of neuromere pixel area, missed 3.5%, and miscalled 0.7%. In contrast, the pure Otsu method detected 60.2% of neuromere pixel area, missed 39.8%, and miscalled 0.6%. The pure Otsu thresholding method is therefore more conservative and detected smaller neuromere regions in the data set.

Generating Seed Lines of Neurites

The patterns of neurites in primary cultures are important morphological features, but can be very complicated (Fig. 2). Traditional edge detection algorithms (e.g., Canny (Canny 1986), Sobel (Gonzalez and Woods 2002), Prewitt (Gonzalez and Woods 2002), Roberts (Gonzalez and Woods 2002), Laplacian of a Gaussian (Gonzalez and Woods 2002), Zero-Crossings (Gonzalez and Woods 2002), etc.) poorly localize neurites because of large ranges in neurite widths and intensity in culture images. We require an approach that accurately localizes neurites yet is invariant to illumination and contrast changes. Instead of directly detecting complete neurites, which is challenging, we make use of the observation that bilateral symmetry is an inherent feature of a line, and compute symmetry information to generate reliable seed lines for neurites, which will then be extended to produce complete neurites using the neurite tracing method described later.

We use an approach proposed by Kovesi (1997) to reliably measure symmetry by integrating local phase information across multiple scales in the frequency domain. At each scale, the difference between the cosine and sine of the phase is computed. The overall symmetry is the normalized summation of the above differences weighted by the total magnitude of the filter responses at the corresponding scales. Let M_n^e and M_n^odenote the even-symmetric (cosine) and odd-symmetric (sine) log Gabor wavelet of scale n. The real and imaginary parts of the responses of an image $I(\mathrm{x})$ to M_n^e and M_n^o are $e_n(x) = I(x)*M_n^e$ and $o_n(x) = I(x)*M_n^o$, respectively. The amplitude and the phase of that Gabor wavelet can be expressed as $A_n(x) = \sqrt{e_n(x)^2 + o_n(x)^2}$ and $\varphi_n(x) = atan2(e_n(x), o_n(x))$, respectively. Symmetry can be quantified as the difference between the absolute value of the even-symmetric filter output and that of the odd-symmetric filter output. To integrate information from filter responses over multiple scales, the amplitude $A_n(x)$ is used to weigh the difference of the absolute values of the even and old filter responses. The final symmetry measure is calculated as the weighted differences normalized by the sum of A_n over all scales:

$$
\begin{aligned}
Sym(x) &= \frac{\sum_n \lfloor A_n(x)[|\cos(\varphi_n(x))| - |\sin(\varphi_n(x))|] - T \rfloor}{\sum_n A_n(x) + \varepsilon} \\
&= \frac{\sum_n \lfloor [|e_n(x)| - |o_n(x)|] - T \rfloor}{\sum_n A_n(x) + \varepsilon}
\end{aligned}
\tag{7}
$$

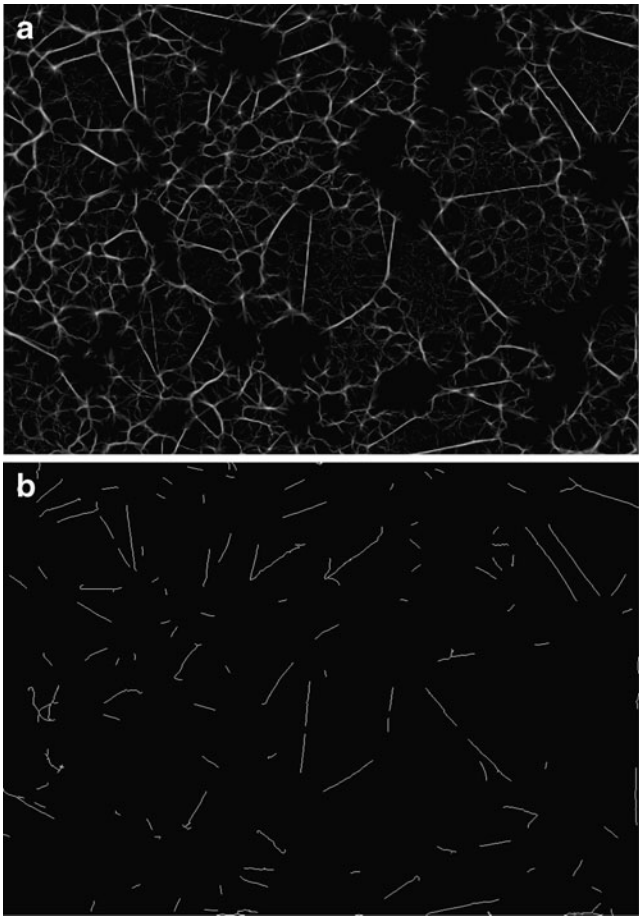

Fig. 6 Phase map and seed lines. **a** The phase map of Fig. 3(a). **b** The seed lines generated from (**a**) by applying binarization, thinning, and morphological operations

where ε is a small value used to avoid dividing by zero and T is the estimated noise compensation that can be obtained by combining the estimated influence of noise on each of the filters. An example is provided in Fig. 6a to show the phase map of Fig. 3a. It was shown that this symmetry measure is independent of the overall magnitude of the signals, which makes it invariant to illumination and contrast changes (Kovesi 1997). Moreover, use of the difference between the cosine and sine of the phase at multiple scales produces a more localized response. This produces better edge localization information, which allows accurate localization of neurites that have a wide range of widths.

Based on the practice reported in (Kovesi 1999), we empirically adjusted the parameters for computing the local symmetry of our images as follows. The number of wavelet scales and the number of filter orientations were set to 5 and 6, respectively. The wavelength of the smallest scale filter was set to 3. The filter bandwidth was set to 0.55. The scaling factor between successive filter rings, which are related to the ratio of the standard deviation of the Gaussian describing the log Gabor filter's transfer function in the frequency domain to the filter centre frequency (i.e., the filter bandwidth), was determined empirically to be 2.0. The ratio of the angular interval between filter orientations and the standard deviations of the angular Gaussian spreading function was determined to be 1.2. The above setting creates a set of wavelets that form a band-pass filter suitable for detecting neurites with a wide range of widths (1 to 8 pixels). Although the above phase symmetry method is very powerful in locating neurites of weak signals, it can sometimes be sensitive to noise. To remove such effects, we binarize the phase symmetry map by using the Otsu thresholding method (Otsu 1979), which is followed by a thinning operation (using the "bwmorph" function in Matlab). Short structures with less than 10 pixels are removed to produce reliable seed lines corresponding to neurite segments. This approach allows a majority of neurites to be subjected to tracing.

Neurite Tracing

To generate a complete neurite map from neurite seed lines, we developed an orientation-guided neurite tracing algorithm that extends the seed lines in the original gray-scale image (Fig. 1d). Neurites are not traced in the phase symmetry map because tracing can be easily digressed by the phase symmetry information of nearby non-neuronal cells and noise. An orientation map (Fig. 7) can be computed using local gradient information because the local orientation of a neurite is usually consistent with that of its neighborhood and is perpendicular to its local gradient. We first computed the local gradient vectors $[G_x, G_y]^T$ by convolving the image with the derivatives of a Gaussian smoothing kernel. The local orientation at (x, y)

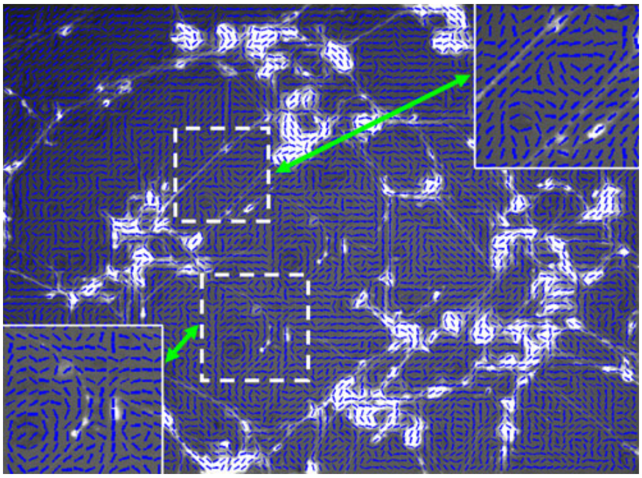

Fig. 7 A gradient-based orientation map is superimposed on the original image. Short blue vectors indicate local orientations. Two regions are zoomed in at the top-right and bottom-left corners to provide more details

was then estimated by finding the principal axis of the autocovariance matrix of $[G_x, G_y]^T$ (Bazen and Gerez 2002), which was defined over a $w \times w$ window as:

$$\Lambda = \begin{bmatrix} G_{xx} & G_{xy} \\ G_{xy} & G_{yy} \end{bmatrix} = \sum_{w} \begin{bmatrix} G_x^2 & G_x G_y \\ G_x G_y & G_y^2 \end{bmatrix} \tag{8}$$

Another popular approach for estimating local orientations is the eigen-decomposition of the Hessian matrix computed at every pixel (Steger 1998), which was used to trace neurites (Xiong et al. 2006; Fan et al. 2009). These two methods generated comparable results when applied to our data. To further reduce the inconsistencies caused by noise, non-neuronal cells, and neuromeres, we applied a low-pass filter to smooth the orientation field:

$$\Phi_x^s(i,j) = \sum\nolimits_{s=-w/2}^{w/2} \sum\nolimits_{t=-w/2}^{w/2} LP(s,t)\Phi_x(i-s, j-t) \tag{9}$$

$$\Phi_y^s(i,j) = \sum\nolimits_{s=-w/2}^{w/2} \sum\nolimits_{t=-w/2}^{w/2} LP(s,t)\Phi_y(i-s, j-t) \tag{10}$$

where i and j are the coordinates, $LP(s, t)$ is a two-dimensional low-pass filter (Hong et al. 1998), and Φ_x and Φ_y are the sine and cosine of the doubled angle of the local gradient and can be computed respectively as:

$$\Phi_x = \frac{G_{xy}}{\sqrt{G_{xy}^2 + (G_{xx} - G_{yy})^2}} \text{ and} \tag{11}$$

$$\Phi_y = \frac{G_{xx} - G_{yy}}{\sqrt{G_{xy}^2 + (G_{xx} - G_{yy})^2}}$$

The gradients of two ridge sides represent the same ridge orientation, however, with opposite directions. Directly averaging them will result in their cancellation. Therefore, to avoid the cancellation problem, the above smooth operation is applied to the doubled angles of the local gradients. This method was proposed in (Kass and Witkin 1987). The final local orientation at position (i, j) is computed by:

$$o(i,j) = \frac{\pi}{2} + \frac{1}{2} \arctan\left(\frac{\Phi_y^s(i,j)}{\Phi_x^s(i,j)}\right) \tag{12}$$

To efficiently trace neurites, we discretized the continuous local orientation (ranging from 0° to 180°) into four directions: horizontal – [0° to 22.5°] ∪ [157.5°, 180°]; negative diagonal – [22.5°, 67.5°]; vertical – [67.5°, 112.5°]; and positive diagonal – [112.5°, 157.5°]. When applied to our data set, this simplification produced results that were comparable to those generated by using 16 or 32 directions as suggested previously (Al-Kofahi et al. 2003).

Our tracing method uses a strategy similar to the non-maximum suppression method of the Canny edge detector (Canny 1986). It traces along the local direction, exploits points where the gradient magnitude is sliced along the gradient direction, marks points where the magnitude is maximal, and finally links the marked points to form neurites. Our tracing method uses a kernel of $H \times K$, where H and K are the width and height of the kernel, respectively. We set H=3 and K=5 in our experiments. Given an end-point from which a neurite segment should be extended, a kernel is placed along the local orientation of that point (Fig. 8). The kernel decides the search range of the target point, which is defined as the point with maximum gray-level intensity within the kernel. A line is then generated to link the current point and its target points. This strategy allows the linkage of neurites that have been broken due to noise (Fig. 8a) and can follow neurites with high curvature (Fig. 8b). The mechanism to extract neurites with high curvature is illustrated in Fig. 8 and is explained as follows. The white "+" denotes the current point close to the high-curvature segment, to which the green kernel is positioned along with the local direction (yellow arrow). The next point (orange dot) is chosen as the foreground pixel with the highest intensity value within the green kernel. If there are multiple best candidate points, the one farthest from the current point will be chosen. The next template (in red) is then aligned with the orange dot. The above design can reliably trace a neurite with high-curvature. Tracing will stop if one of the following conditions is met: (1) an image boundary is reached; (2) a neuromere or neurite is reached; and (3) the maximum intensity within the kernel is below a threshold value. Examples of neurite extraction results are illustrated in Fig. 9.

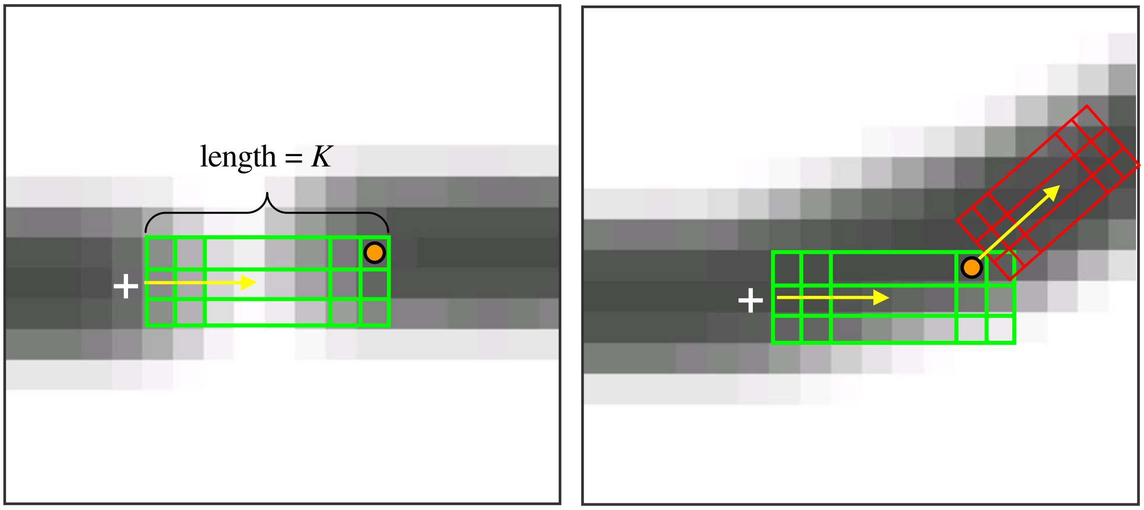

(a) (b)

Fig. 8 The neurite tracing mechanism using kernels (**a**) to link broken neurite segments due to noise or (**b**) to trace neurites along segments with high curvature. (**a**) To extend a broken neurite segment, a kernel (green template) initiates a search range from the current point (+), which is the endpoint of the broken neurite, along its local direction (yellow arrow). The target point (orange dot) is defined as the point with maximum gray-level intensity within the kernel. A line is then generated to link the current point and its target point. If there are multiple best candidate points, the one farthest from the current point will be chosen. (**b**) When tracing curved neurite segments, the next kernel (red template) for searching the next target point of the current target point (orange dot) forms a sharp angle with the current kernel (green template). Tracing will stop if one of the following conditions is met: (1) an image boundary is reached; (2) a neuromere or neurite is reached; and (3) the maximum intensity within the kernel is below a threshold value

Comparing Morphological Profiles Between Different Conditions

To statistically compare the morphologies of different neuronal cell cultures, we needed to derive a set of morphological features that characterize any given culture. Several morphological features have been proposed for studying the morphology of individual neurons (Costa Lda et al. 2002; Rocchi et al. 2007; Leandro et al. 2009). Nevertheless, those features are not appropriate for describing primary cultures since they contain complicated networks of many intertwining neuronal cells. We therefore designed the following set of morphological features to characterize the primary neuronal cell culture in each image.

First, neuromeres were discretized into three types based on their sizes (i.e., number of pixels): small, medium, and large. This was done by fitting a Gaussian mixture model (GMM) (Duda et al. 2000) to the distribution of the logarithm of neuromere sizes using the Expectation and Maximization algorithm (Dempster et al. 1977). Approximately sixty-six thousand neuromeres from 1,700 randomly selected images were used for fitting the GMM. The final GMM has three components representing small, medium, and large neuromeres, respectively:

$$p(x) = \sum_{m=1}^{3} p_m f\left(x|\mu_m, \sigma_m^2\right) \tag{13}$$

where x is the logarithm of a neuromere size, p_m, μ_m, and $\sigma_m{}^2$ are the component probability, mean, and variance of the m-th component and $\Sigma_m\, p_m=1$. The GMM assigns a cluster to each neuromere by choosing the component with the largest posterior probability, weighted by the component probability. Figure 10 illustrates the GMM fitting result using our data. Neuromeres were clustered into three categories: small size ($\log(\text{area}) \le 5.06$), medium size ($5.06 < \log(\text{area}) \le 6.32$), and large size ($\log(\text{area}) > 6.32$). We then applied K-means (Duda et al. 2000) to the lengths (in pixels) of approximately 612,000 neurite branches in the same image set to produce three groups: short ($\text{length} \le 42.53$), medium ($42.53 < \text{length} \le 107.03$), and long ($\text{length} > 107.03$). Since cell numbers can vary slightly from well to well due to pipetting error, the absolute counts of morphological features per well can also vary. To overcome this problem, we converted the absolute feature counts into percentages, and used three neuromere features representing the percentages of small, medium, and large neuromeres, three neurite features representing the percentages of short, medium, and long neurites, and other features such as the average of the logarithm of neuromere areas and the average length of neurites.

To compare neuron morphology between different cell cultures including those Htt-Q15 and Htt-Q138 expressing cells, the p-value of each individual morphological feature was first computed by applying the two sample t-test to compare its populations in two given conditions. The p-values of the individual features were then combined into

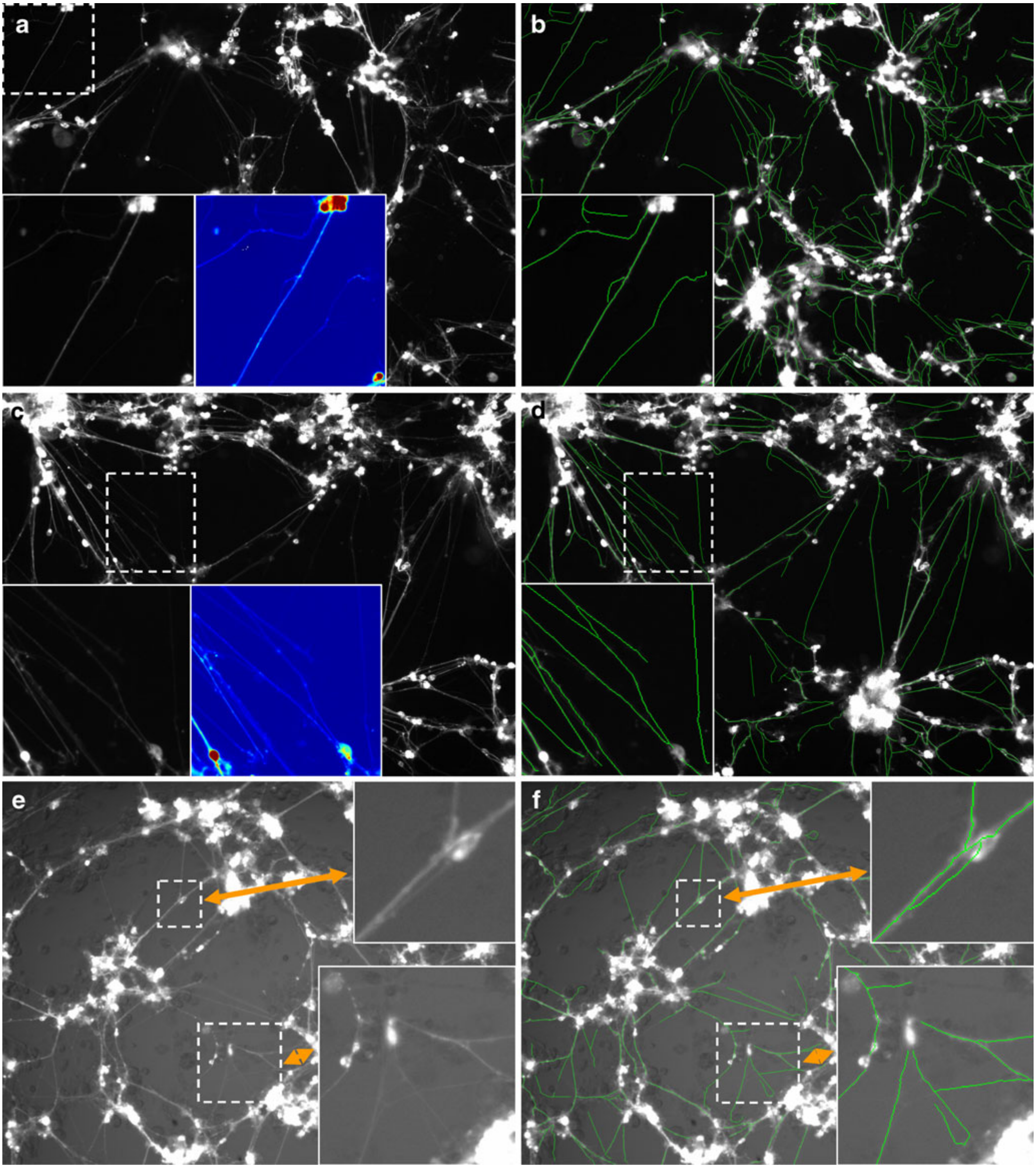

Fig. 9 Neurite extraction examples. **a**, **c**, and **e** are the original images with regions zoomed in to provide more details. The pseudo-color of the zoom-in regions are provided in (**a**) and (**c**) to make the faint neurites visually more perceptible. **b**, **d**, and **f** are the neurite extraction results (in green) overlapping with the original images. **b** and **d** show that our method is capable of accurately extracting faint neurites. **f** shows that the proposed method appropriately recognizes branching points in complicated structures

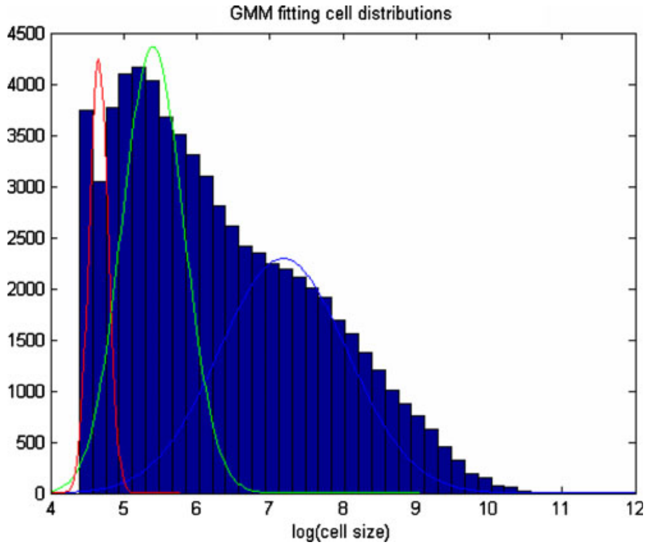

Fig. 10 Categorizing segmented neuromeres using a Gaussian mixture model. The vertical axis denotes the numbers of neuromeres. The horizontal axis denotes the logarithm of neuromere sizes. The GMM trained by the Expectation Maximization algorithm has three components representing small (red), medium (green), and large (blue) neuromeres. The priors, means, and variances of those three Gaussian components are (0.17, 4.79, 0.07), (0.35, 5.62, 0.28), and (0.48, 7.37, 1.17), respectively

one single morphology *p*-value using the Stouffer method (Hedges and Olkin 1985). A lower morphology *p*-value indicates a higher degree of dissimilarity between the cell cultures of two treatment conditions. The Stouffer method is one of several commonly used methods for combining *p*-values in meta-analysis. It first takes a transformation $H(\cdot)$ of *p*-values and then evaluates the sum of the transformed *p*-values $Y = \sum_{i=1}^{T} H(p_i)$, where T is the total number of tests and p_i is the *p*-value of the *i*-th test. An inverse standard normal cumulative distribution function is used so that the cumulative distribution function of Y is normal. This method works well in cases where the evidence against the null-hypothesis is spread across different attributes.

For each individual image, the number of independent neuromere features is two because three neuromere features sum up to 100%. Nevertheless, we cannot arbitrarily remove one of those three features in our statistical analysis on morphological differences. For example, it is possible that a treatment has two neuromere features whose means are smaller, however, not statistically significant, than their counterparts of the negative Htt-Q15 control. Nevertheless, the mean of its third neuromere feature can be statistically significantly larger than that of the negative Htt-Q15 control. In such scenario, relying solely on the first two neuromere features will lead to the failure in detecting the significant difference in the neuromere feature category as a whole. This can also happen to the neurite feature category. Therefore, all features are included in our morphological *p*-value calculation.

Assessing Htt Aggregation

To assess Htt aggregation, we first extracted Htt aggregate signals from Htt-mRFP (Cy3 channel) images. We binarized each Htt-mRFP image by simply classifying pixels with intensity (ranging from 0 to 1) larger than an empirically decided threshold (=0.3) into the foreground representing Htt protein aggregates. The Htt aggregate density of the Htt-RFP image was defined as the ratio between the total area of Htt aggregates and the total cell area in the corresponding GFP labelled image. The two sample *t*-test was used to compare the Htt aggregate density values for Htt-Q138 and control Htt-Q15. A small *t*-test *p*-value indicates differences in Htt protein aggregation between the two conditions.

Results

Comparison, Evaluation and Robustness Study

During the course of this study, two comparable state of the art software packages were publically available: HCA-Vision (Sun and Vallotton 2009) (http://www.hca-vision.com/) and NeuriteIQ (http://www.cbi-tmhs.org/NeuriteIQ/index.htm). Both software packages provide automatic neurite extraction functionalities, which were made available after we finished the development of our approach and the analysis of the *Drosophila* HD data set. However, neither of them provided functionalities for statistically analyzing the significance of the morphological differences between different treatment conditions, which is one of our contributions. For our comparison analysis, we used the trial version of HCA-Vision ver 2.0.0, which allows full access for 30 days, and the latest version of NeuriteIQ as of 12/01/2009. We tried all built-in parameter settings provided by HCA-Vision and decided that the NH14 setting generated the best results for the *Drosophila* HD data set. Neurite extraction using the default setting of HCA-Vision was very sensitive to the complex local gradient profiles around neuromeres and the non-neuronal cells in the *Drosophila* HD data set. The default setting of NeuriteIQ was used. A comparison example is shown in Fig. 11 for visual assessment.

A qualitative test was performed to evaluate how well HCA-Vision, NeuriteIQ, and our approach can deal with neurites which are faint or contain faint segments. Twenty-five image regions (256×256 pixels) were randomly selected from the *Drosophila* HD data set. There were 123 neurite segments (long or medium) of interest in those image regions, which were important for assessing the health of cell cultures. Two neurobiologists among the authors (J.S. and K.S.) manually examined neurites

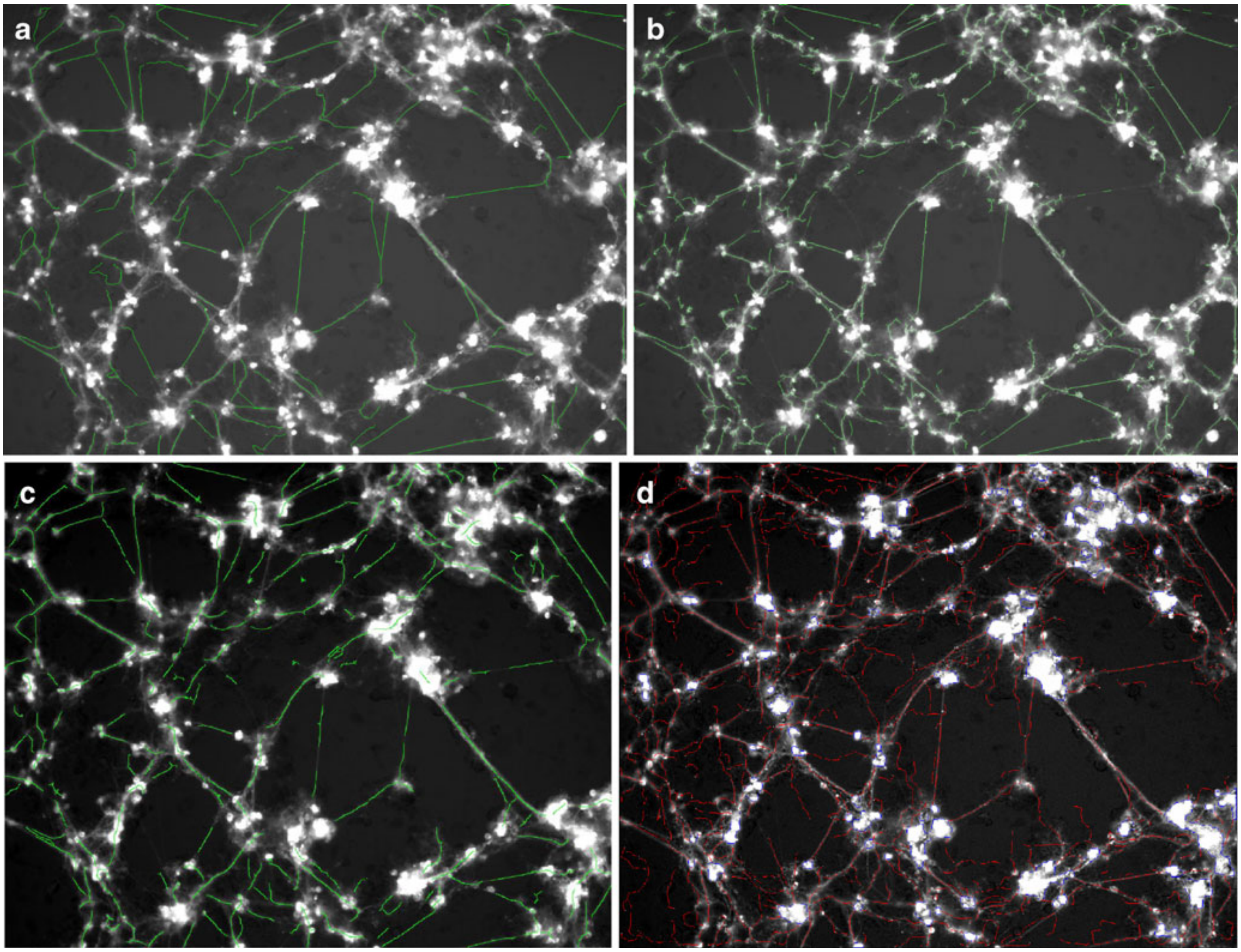

Fig. 11 Comparing neurite extraction results. The original image is Fig. 3a. The neurite extraction results of (**a**) our approach (neurites in green), **b** HCA-vision using the NH14 parameter setting (neurites in green), **c** NeuriteIQ using the curvilinear algorithm (neurites in green), and (**d**) NeuriteIQ using the dynamic programming algorithm* (neurites in red). The image was cropped to 1280×1024 in (**c**) and (**d**) as required by NeuriteIQ. *This method is not in the current public version of NeuriteIQ

extracted by the above three approaches and grouped them into "good", "broken", and "missed" categories. A neurite extraction result was classified as "good" if it matched the expectation of both experts, "broken" if it was broken into two or more major segments or was significantly shorter than expected, or "missed" if a method simply failed to detect a neurite segment because it was too faint. The results (Table 1) indicate that our approach results in the generation of fewer broken neurite segments as compared to NeuriteIQ or HCA-Vision. However, the numbers of neurites "missed" by all three approaches are substantial, which indicate that the images are quite challenging and future improvements of existing methods are needed to fully address this issue.

Table 1 Qualitative comparison

	Good	Broken	Missed
The proposed approach	106	2	15
NeuriteIQ (default setting)	86	21	16
HCA-vision (NH14)	79	33	11

We also quantitatively evaluated the capability of our method to localize the central lines of neurites. Two neurobiologists independently labelled 106 neurite segments (with minimal and maximal length of 49 and 278 pixels, respectively) that were extracted by our method as "good" ones (see Table 1). The "broken" and "missed" ones were treated as failures and were not used in this evaluation. To reduce the effects of human bias, we adopted a strategy proposed by Zhang et al. (Zhang et al. 2007) and asked both experts to label the central lines of neurites by using the starting and ending points detected by our

Table 2 Quantitative evaluation of the proposed approach

	d_1 (mean/std)	d_2 (mean/std)
our approach *vs* biologist 1	0.011/0.007	0.499/0.095
our approach *vs* biologist 2	0.012/0.008	0.544/0.094
biologist 1 *vs* biologist 2	0.01/0.007	0.511/0.092

approach. The length difference between an automatically extracted neurite (l_a) and the manually labelled one (l_m) is defined as $d_1 = |l_m - l_a|/l_a$ (Zhang et al. 2007). To compute the difference (d_2) between an automatically extracted central line and its counterpart labelled manually, we first used the dynamic time warping package (Ellis 2003) and its default parameter setting to align the neurites extracted automatically to those labelled manually, and then computed the average Euclidean distance (in pixels) between the matching point pairs. The neurite detection results of our approach were consistent to those manually extracted by both experts (Table 2).

To test the robustness of our method with respect to noise, we created a clean synthetic image (Fig. 12a) based on Fig. 9e, and then added zero-mean Gaussian noise with different variances. We chose Gaussian noise distributions because the local noise distributions in both the original images and the background-corrected ones were Gaussian alike. The neurites of the synthetic image have typical characteristics (e.g., strong, weak, thick, thin, curved, and with branching points) of those in the raw images. In this test, we were more concerned about the breakage of long neurites into smaller segments and missing neurites because such errors often change the category of a neurite. The local signal-to-noise-ratio (SNR) ranges from 1.81 to 14.3 in the synthesized image. The local SNR is defined over a 9×9 pixel region as the ratio between the mean of the true signal (without counting neuromeres) within that region and the standard deviation of the noise. Our method can robustly detect most neurites with virtually no false detection in this noisy setting (Fig. 12b). Nonetheless, it produces noticeable failures in the areas where local SNR is lower than 3.8 (e.g., the zoomed-in in Fig. 12b).

Analyzing the *Drosophila* HD Data Set

Our approach was applied to the *Drosophila* HD data set to identify morphological differences induced by Htt-Q138 expression compared to control Htt-Q15 expression. Figure 13 shows the exemplar images of the neuronal cell cultures from Htt-Q15 and Htt-Q138. The morphological *p*-value for Htt-Q138 was computed with respect to the negative Htt-Q15 control. Our approach did show that the morphology of untreated pathogenic Htt-Q138 cultures was indeed significantly distinct from that of non-pathogenic Htt-Q15 cultures (morphological p-value $<10^{-50}$). This is in agreement with neurobiologists (J.S. and K.J.S) who can readily tell the differences in the morphology of the two cultures by visual inspection.

This striking difference in morphology induced by pathogenic Htt and the ability of our computational approach to detect such difference allowed us to begin a large-scale HCS screen for potential compounds that could revert the neuronal morphology profiles associated with mutant Htt-Q138 expression towards that of the healthy

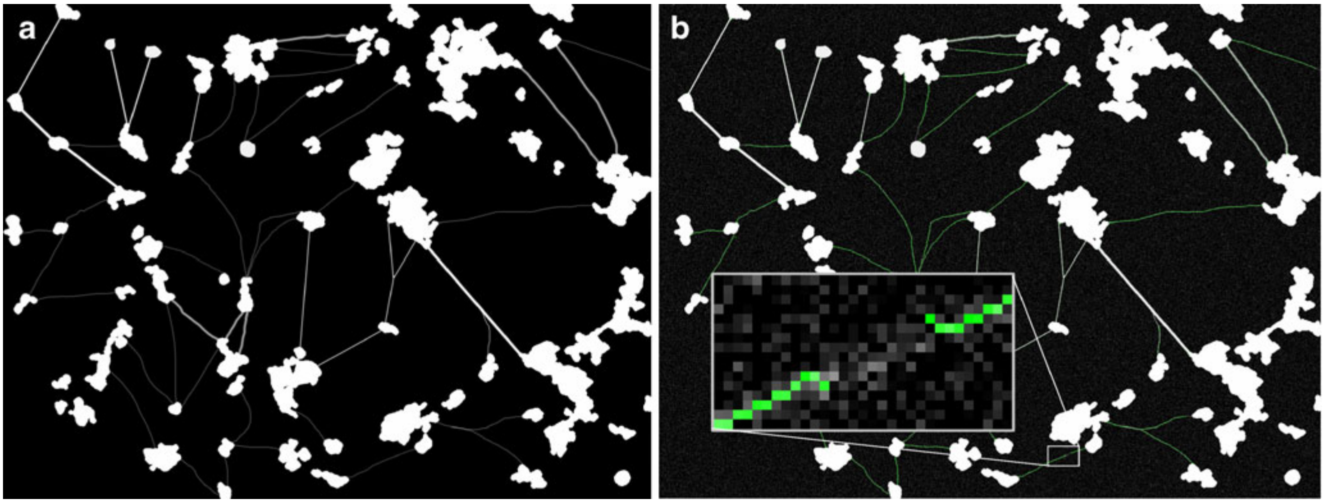

Fig. 12 Robustness test using a synthetic image. **a** The synthetic clean image (without noise) contains neurites of different characteristics, such as wide/narrow, strong/weak, straight/curved, and so on. **b** The detected neurites (in green) are superimposed on the synthetic noisy images. Our approach successfully detected most neurites. However, it failed to detect weak neurite segments where the local SNR is lower than 3.8. A failure case is zoomed-in

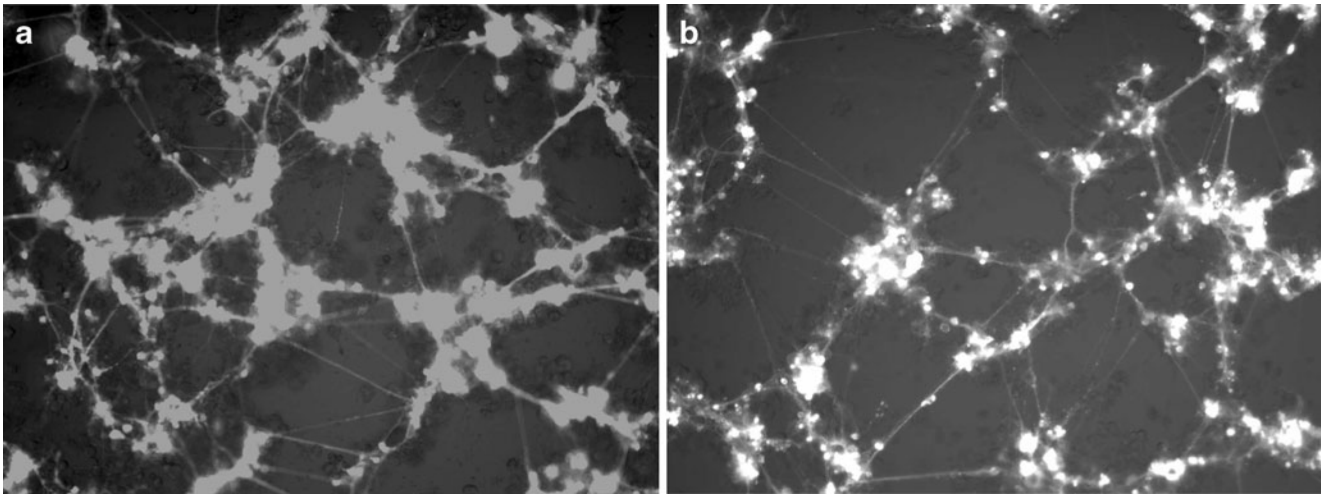

Fig. 13 Exemplar images of Htt-Q15 (**a**) and Htt-Q138 (**b**)

negative control expressed with wild-type Htt. A relatively large morphological *p*-value is a necessary condition for calling a compound as a hit. That is the morphological profile of a hit should not be significantly different from that of the negative Htt-Q15 control. In addition to altered morphology induced by Htt-Q138, we assessed aggregation of pathogenic Htt protein within neurons given that protein aggregation is a hallmark of the polyglutamine diseases. Htt aggregation inhibition ratios were computed with respect to the mutant cultures without treatment. A hit should also show a significant Htt aggregation inhibition ratio. In preliminary studies of approximately 1800 chemical compounds, ~30 compounds significantly inhibited Htt aggregation (*p*-value <0.001), and two hits had significant improvement of neurite morphology (with morphological *p*-values equal to 0.1143 and 0.1124, respectively) in addition to significant inhibition of Htt protein aggregates (with mean ratios equal to 37.0 and 17.8, respectively; *p*-values equal to 9.2×10^{-5} and 1.59×10^{-4}, respectively). The morphological test results were visually confirmed by two neurobiologists (J.S. and K.J.S.), therefore demonstrating the power of our approach to identify distinct morphological differences in the *Drosophila* HD cultures. Future studies will test the efficacy of these compounds in vivo for their effects on Htt-Q138 toxicity.

In Tables 3 and 4, we list the statistics of a few morphological features that differed between Htt-Q15 and Htt-Q138 expressing neurons.

Computation Time

Our method takes about 40 s to extract neurites in one image using one core on a Dell 64-bit PE2950 server (two quad-core Intel® Xeon® E5410 processors @2.33GHZ and 8.00 GB memory) running 64-bit Windows Server 2008 operating system.

Conclusion and Discussion

The novelties of our method can be summarized as the following. Image quality is enhanced by correcting uneven backgrounds. The adverse effects on neurite extraction by complex gradient patterns of neuromeres are removed through efficient texture segmentation. By using phase-based symmetry information, our method offers a major advantage over existing methods in accurately localizing neurites and detecting faint neurites in noisy backgrounds. We also designed a set of morphological features and a statistical analysis method to quantitatively compare the morphology of neuronal cell cultures expressing non-pathogenic Htt-Q15 and pathogenenic Htt-Q138 under different treatment conditions. To the best of our knowledge, our method is the first one being employed to analyze such large data sets. The results suggest that it can be a powerful tool in high-throughput screening image analysis and computer-aided drug discovery. Since the degenerative

Table 3 Example statistics of neuromeres. The size of a neuromere is measured as the total number of its pixels. The 2nd, 3rd, and 4th columns are the percentages of small, medium, and large cells, respectively

	log(cell size) mean (std)	Small cells % Mean (std)	Medium cell % mean (std)	Large cell % mean (std)
Htt-Q15	6.31 (1.33)	19.4 (4.2)	36.8 (4.7)	43.8 (5.0)
Htt-Q138	5.96 (1.50)	31.8 (3.1)	28.8 (3.6)	39.4 (3.8)

Table 4 Example statistics of neurite branches. The length of a neurite is measured in pixels. The 2nd, 3rd, and 4th columns are the percentages of short, medium, and long neurites, respectively

	Length (pixels) mean (std)	Short Neurite % mean (std)	Medium Neurite % mean (std)	Long Neurite % (std)
Htt-Q15	24.99 (18.93)	81.0 (1.7)	17.4 (1.6)	1.6 (0.6)
Htt-Q138	26.12 (21.33)	78.7 (1.8)	18.9 (1.7)	2.4 (0.5)

HD model shares many characteristics with other neurodegenerative diseases such as Alzheimer's and Parkinson's Diseases, we expect that the quantification and statistical analysis methods presented here should be readily transferable to many other neuronal HCS screening platforms related to neuronal degeneration.

The parameters of our image processing pipeline presented in this paper may need to be re-tuned for neuronal cell cultures of different origins. For example, different species may have quite different neuronal cell body sizes. This can affect the choice of the structuring element used by the neuromere segmentation component to remove small regions corresponding to noise via an image morphological operation. The texture-based neuromere segmentation component may be dispensable or can be simplified greatly if the cell cultures are simpler. For example, other neuronal cell culture models may not form complex clusters and may not contain non-neuronal cells that are closely associated with neuronal cells. The non-neuronal cells in our cultures are known to be biologically very important for supporting neuronal cells. Other issues such as image resolution and optical objective, which directly affect the sizes/widths of objects in images, can also affect the values of some parameters (e.g., the tile size used in the CLAHE method, the window size used in the texture analysis, the wavelengths used in computing symmetry information, and the length of the kernel used in neurite tracing). Based on our experience, we expect that the amount of time required for tuning those parameters should be reasonably small. It took us around one day to tune all parameters the first time around using the *Drosophila* HD data set (discounting time for software development and choosing appropriate combinations of image processing components). Recently, it took us approximately one hour to adjust our neurite extraction approach for an HCS project (Schoemans et al. in press) using mouse neuronal cell cultures, which were quite different from those used to generate the *Drosophila* HD data set. Finally, while high-content screens of neuronal cell cultures are attracting more and more attention, many new protocols may be developed for preparing neuronal cell cultures for various experimental paradigms, which may require future adjustments of existing methods or developing new processing components to account for new analysis requirements.

The morphological p-values generated by our approach may be used to guide the identification of toxic treatments. For example, a small morphological p-value plus an abnormally high percentage of short neurites may indicate that a treatment is toxic to neuronal cell cultures. Visual examination by experimental experts is required to confirm such toxicity hypotheses. A quantitative relationship between the toxicity of a treatment and its morphological p-value and features may be established if enough bench data from experiments on toxicity of treatments is available.

Information Sharing Statement

The image data used in this work are provided by The Picower Institute for Learning and Memory, Departments of Biology and Brain and Cognitive Sciences, Massachusetts Institute of Technology. Our software was developed using Matlab and requires the image processing toolbox and the statistical analysis toolbox. The source codes are available upon request.

Acknowledgement CW and PH are supported by an NIH to PH. JS and JTL are supported by an NIH grant to JTL. We appreciate the kind help of Dr. Xiaobo Zhou and Dr. Shi Peng at the Weill Medical College of Cornell University in using their NeuriteIQ software to generate the neurite tracing results shown in Fig. 11c and d.

References

Al-Kofahi, K., Lasek, S., Szarowski, D., Pace, C., Nagy, G., Turner, J. N., et al. (2002). Rapid automated three-dimensional tracing of neurons from confocal image stacks. *IEEE Transactions on Information Technology in Biomedicine, 6*(2), 171–187.

Al-Kofahi, K. A., Can, A., Lasek, S., Szarowski, D. H., Dowell-Mesfin, N., Shain, W., et al. (2003). Median-based robust algorithms for tracing neurons from noisy confocal microscope images. *IEEE Transactions on Information Technology in Biomedicine, 7*(4), 302–317.

Bazen, A. M., & Gerez, S. H. (2002). Systematic methods for the computation of the directional fields and singular points of fingerprints. *IEEE Transactions on Pattern Analysis and Machine Intelligence, 24*(7), 905–919.

Boland, M. V., & Murphy, R. F. (1999). Automated analysis of patterns in fluorescence-microscope images. *Trends in Cell Biology, 9*(5), 201–202.

Boland, M. V., & Murphy, R. F. (2001). A neural network classifier capable of recognizing the patterns of all major subcellular structures in fluorescence microscope images of HeLa cells. *Bioinformatics, 17*(12), 1213–1223.

Boland, M. V., Markey, M. K., & Murphy, R. F. (1998). Automated recognition of patterns characteristic of subcellular structures in fluorescence microscopy images. *Cytometry, 33*(3), 366–375.

Broser, P. J., Erdogan, S., Grinevich, V., Osten, P., Sakmann, B., & Wallace, D. J. (2008). Automated axon length quantification for populations of labelled neurons. *Journal of Neurosci Methods, 169*(1), 43–54.

Canny, J. (1986). A computational approach to edge detection. *IEEE Transactions on Pattern Analysis and Machine Intelligence, 8*(6), 679–698.

Carpenter, A. E. (2007). Image-based chemical screening. *Nature Chemical Biology, 3*(8), 461–465.

Chen, X., & Murphy, R. F. (2006). Automated interpretation of protein subcellular location patterns. *International Review of Cytology, 249*, 193–227.

Costa Lda, F., Manoel, E. T., Faucereau, F., Chelly, J., van Pelt, J., & Ramakers, G. (2002). A shape analysis framework for neuromorphometry. *Network, 13*(3), 283–310.

Daugman, J. G. (1985). Uncertainty relations for resolution in space, spatial frequency, and orientation optimized by two-dimensional visual cortical filters. *Journal of the Optical Society of America A, 2*, 1160–1169.

Dempster, A. P., Laird, N. M., & Rubin, D. B. (1977). Maximum likelihood from incomplete data via the EM algorithm (with discussion). *Journal of the Royal Statistical Society Series B (Methodological), 39*(1), 1–38.

Dragunow, M. (2008). High-content analysis in neuroscience. *Nature Reviews. Neuroscience, 9*(10), 779–788.

Duda, R., Hart, P., & Stork, D. (2000). *Pattern classification* (2nd ed.). New York: Wiley.

Eggert, U. S., & Mitchison, T. J. (2006). Small molecule screening by imaging. *Current Opinion in Chemical Biology, 10*(3), 232–237.

Eggert, U. S., Kiger, A. A., Richter, C., Perlman, Z. E., Perrimon, N., Mitchison, T. J., et al. (2004). Parallel chemical genetic and genome-wide RNAi screens identify cytokinesis inhibitors and targets. *PLoS Biology, 2*(12), e379.

Ellis, D. (2003). “Dynamic Time Warp (DTW) in Matlab.” from http://www.ee.columbia.edu/~dpwe/resources/matlab/dtw/.

Fan, J., Zhou, X., Dy, J. G., Zhang, Y., & Wong, S. T. (2009). An automated pipeline for dendrite spine detection and tracking of 3D optical microscopy neuron images of in vivo mouse models. *Neuroinformatics, 7*(2), 113–130.

Fredieu, J. R., & Mahowald, A. P. (1989). Glial interactions with neurons during Drosophila embryogenesis. *Development, 106*(4), 739–748.

Gonzalez, R. C., & Woods, R. E. (2002). *Digital image processing*. Prentice Hall.

González, R. C., & Woods, R. E. (2007). *Digital image processing*. Prentice Hall.

Grigorescu, S. E., Petkov, N., & Kruizinga, P. (2002). Comparison of texture features based on Gabor filters. *IEEE Transactions on Image Processing, 11*(10), 1160–1167.

Hedges, L., & Olkin, I. (1985). *Stat. Method meta-analysis*. San Diego: Academic.

Hong, L., Wan, Y., & Jain, A. (1998). Fingerprint image enhancement: algorithm and performance evaluation. *IEEE Transactions on Pattern Analysis and Machine Intelligence, 20*(8), 777–789.

Kass, M., & Witkin, A. (1987). Analyzing oriented patterns. *Computer Vision, Graphics, and Image Processing, 37*(3), 362–385.

Kimura, Y., Lee, W. C., & Littleton, J. T. (2007). Therapeutic prospects for the prevention of neurodegeneration in Huntington's Disease and the polyglutamine repeat disorders. *Mini Reviews in Medicinal Chemistry, 7*, 99–106.

Kovesi, P. (1997). Symmetry and asymmetry from local phase. Tenth Australian Joint Conference on Artificial Intelligence, pp. 185–190.

Kovesi, P. (1999). Image features from phase congruency. *Videre: A Journal of Computer Vision Research*, 1(3).

Leandro, J. J., Cesar, R. M., Jr., & Costa Lda, F. (2009). Automatic contour extraction from 2D neuron images. *Journal of Neurosci Methods, 177*(2), 497–509.

Liebel, U., Starkuviene, V., Erfle, H., Simpson, J. C., Poustka, A., Wiemann, S., et al. (2003). A microscope-based screening platform for large-scale functional protein analysis in intact cells. *FEBS Letters, 554*(3), 394–398.

Meijering, E., Jacob, M., Sarria, J. C., Steiner, P., Hirling, H., & Unser, M. (2004). Design and validation of a tool for neurite tracing and analysis in fluorescence microscopy images. *Cytometry A, 58*(2), 167–176.

Mitchison, T. J. (2005). Small-molecule screening and profiling by using automated microscopy. *Chembiochem, 6*(1), 33–39.

Muller, P., Kuttenkeuler, D., Gesellchen, V., Zeidler, M. P., & Boutros, M. (2005). Identification of JAK/STAT signalling components by genome-wide RNA interference. *Nature, 436*(7052), 871–875.

Murphy, R. F., Boland, M. V., & Velliste, M. (2000). Towards a systematics for protein subcelluar location: quantitative description of protein localization patterns and automated analysis of fluorescence microscope images. *Proceedings International Conference on Intelligent Systems for Molecular Biology, 8*, 251–259.

Narro, M. L., Yang, F., Kraft, R., Wenk, C., Efrat, A., & Restifo, L. L. (2007). NeuronMetrics: software for semi-automated processing of cultured neuron images. *Brain Research, 1138*, 57–75.

Neumann, B., Held, M., Liebel, U., Erfle, H., Rogers, P., Pepperkok, R., et al. (2006). High-throughput RNAi screening by time-lapse imaging of live human cells. *Nature Methods, 3*(5), 385–390.

Otsu, N. (1979). A threshold selection method from gray-level histograms. *IEEE Transactions on Systems, Man and Cybernetics, 9*(1), 62–66.

Pelkmans, L., Fava, E., Grabner, H., Hannus, M., Habermann, B., Krausz, E., et al. (2005). Genome-wide analysis of human kinases in clathrin- and caveolae/raft-mediated endocytosis. *Nature, 436*(7047), 78–86.

Peng, H. (2008). Bioimage informatics: a new area of engineering biology. *Bioinformatics, 24*(17), 1827–1836.

Perlman, Z. E., Slack, M. D., Feng, Y., Mitchison, T. J., Wu, L. F., & Altschuler, S. J. (2004). Multidimensional drug profiling by automated microscopy. *Science, 306*(5699), 1194–1198.

Pool, M., Thiemann, J., Bar-Or, A., & Fournier, A. E. (2008). NeuriteTracer: a novel ImageJ plugin for automated quantification of neurite outgrowth. *Journal of Neuroscience Methods, 168*(1), 134–139.

Rocchi, M. B., Sisti, D., Albertini, M. C., & Teodori, L. (2007). Current trends in shape and texture analysis in neurology: aspects of the morphological substrate of volume and wiring transmission. *Brain Research Reviews, 55*(1), 97–107.

Schoemans, R., Aigrot, M. S., Wu, C., Marée, R., Hong, P., Belachew, S., et al.. (in press). Oligodendrocyte development and myelinogenesis are not impaired by high concentrations of phenylalanine or its metabolites. *Journal of Inherited Metabolism Disease*.

Seecof, R. L., Donady, J. J., & Teplitz, R. L. (1973). Differentiation of Drosophila neuroblasts to form ganglion-like clusters of neurons in vitro. *Cell Differentiation, 2*(3), 143–149.

Sepp, K. J., Hong, P., Lizarraga, S. B., Liu, J. S., Mejia, L. A., Walsh, C. A., et al. (2008). Identification of neural outgrowth genes using genome-wide RNAi. *PLoS Genetics, 4*(7), e1000111.

Sonnichsen, B., Koski, L. B., Walsh, A., Marschall, P., Neumann, B., Brehm, M., et al. (2005). Full-genome RNAi profiling of early embryogenesis in Caenorhabditis elegans. *Nature, 434*(7032), 462–469.

Steger, C. (1998). An unbiased detector of curvilinear structures. *IEEE Transactions on Pattern Analysis and Machine Intelligence, 20*(2), 113–125.

Sun, C., & Vallotton, P. (2009). Fast linear feature detection using multiple directional non-maximum suppression. *Journal of Microscopy, 234*(2), 147–157.

Vallotton, P., Lagerstrom, R., Sun, C., Buckley, M., Wang, D., De Silva, M., et al. (2007). Automated analysis of neurite branching in cultured cortical neurons using HCA-Vision. *Cytometry A, 71*(10), 889–895.

Wheeler, D. B., Carpenter, A. E., & Sabatini, D. M. (2005). Cell microarrays and RNA interference chip away at gene function. *Nature Genetics, 37*(Suppl), S25–S30.

Wollman, R., & Stuurman, N. (2007). High throughput microscopy: from raw images to discoveries. *Journal of Cell Science, 120*(Pt 21), 3715–3722.

Xiong, G., Zhou, X., Degterev, A., Ji, L., & Wong, S. T. (2006). Automated neurite labeling and analysis in fluorescence microscopy images. *Cytometry A, 69*(6), 494–505.

Zhang, Y., Zhou, X., Degterev, A., Lipinski, M., Adjeroh, D., Yuan, J., et al. (2007). Automated neurite extraction using dynamic programming for high-throughput screening of neuron-based assays. *Neuroimage, 35*(4), 1502–1515.

Zuiderveld, K. (Ed.). (1994). *Contrast limited adaptive histogram equalization. Graphics gems IV.* Princeton: Academic.